Experimental investigation of the compression and heating of an MHD-driven jet impacting a target cloud

Byonghoon Seo, and Paul M. Bellan

Citation: Physics of Plasmas **25**, 112703 (2018); doi: 10.1063/1.5045678
View online: https://doi.org/10.1063/1.5045678
View Table of Contents: http://aip.scitation.org/toc/php/25/11
Published by the American Institute of Physics

Experimental investigation of the compression and heating of an MHD-driven jet impacting a target cloud

Byonghoon Seo[a] and Paul M. Bellan[b]
Applied Physics, Caltech, Pasadena, California 91125, USA

(Received 22 June 2018; accepted 22 October 2018; published online 7 November 2018)

Adiabatic compression has been investigated by having an MHD-driven plasma jet impact a gas target cloud. Compression and heating of the jet upon impact were observed and compared to theoretical predictions. Diagnostics for comprehensive measurements included a Thomson scattering system, a fast movie camera, a translatable fiber-coupled interferometer, a monochromator, a visible-light photodiode, and a magnetic probe array. Measurements using these diagnostics provided the time-dependent electron density, electron temperature, continuum emission, line emission, and magnetic field profile. Increases in density and magnetic field and a decrease in jet velocity were observed during the compression. The electron temperature had a complicated time dependence, increasing at first, but then rapidly declining in less than 1 μs which is less than the total compression time. Analysis indicates that this sudden temperature drop is a consequence of radiative loss from hydrogen atoms spontaneously generated via three-body recombination in the high-density compressed plasma. A criterion for how fast compression must be to outrun radiative loss is discussed not only for the Caltech experiment but also for fusion-grade regimes. In addition, the results are analyzed in the context of shocks the effects of which are compared to adiabatic compression. *Published by AIP Publishing*. https://doi.org/10.1063/1.5045678

I. INTRODUCTION

Adiabatic compression is of fundamental interest in plasma physics. It is also of particular interest to controlled thermonuclear fusion as this requires heating a plasma to 10 keV while simultaneously satisfying the Lawson criterion for the product of density and energy confinement time. In the quest for attaining controlled fusion, two main approaches, magnetic confinement fusion (MCF) and inertial confinement fusion (ICF), have been used. MCF uses magnetic fields to improve confinement whereas ICF uses compression to increase the density and temperature. Since magnetic field improves plasma confinement while adiabatic compression increases density and temperature, adiabatic compression of a magnetized plasma should exploit virtues of both MCF and ICF. Such adiabatic compression of a magnetized plasma is the basis of magnetized target fusion (MTF, also known as Magneto-Inertial Fusion) wherein an imploding liner adiabatically compresses a magnetized plasma to the density and temperature required for fusion.[1–6] MTF offers the possibility of low-cost fusion by operating in a parameter regime intermediate between MCF and ICF.[4,7]

Fusion-grade MTF experiments now underway have a very limited shot repetition rate because the liner and substantial additional hardware are destroyed in each shot and have to be rebuilt and reinstalled.[8] This destruction greatly limits the number of shots in an experimental campaign and so impedes the investigation and optimization of adiabatic compression.

The Caltech jet-cloud impact experiment was designed to investigate adiabatic compression using a configuration that has a high shot repetition rate and no destruction of hardware. The non-destruction feature in this configuration results from having a high-speed MHD-driven jet[9–11] impact a localized target cloud of heavy gas. An observer in the jet frame would see the target cloud moving towards the jet plasma and then compressing the jet plasma. The plasma parameters in this experiment are much more modest than in a fusion-grade configuration but in compensation, the shot repetition rate of one shot every two minutes is much higher. Since ideal MHD has no intrinsic scale, ideal MHD is capable of describing configurations having many orders of magnitude difference in size.[12] Thus, the compression physics in the Caltech experiment is relevant to fusion-grade configurations because dimensionless parameter ratios can be extrapolated. In addition, radiative processes such as continuum radiation by which particle energy is lost can be investigated using the repetitive and non-destructive scheme. Moser and Bellan[11] observed magnetic flux compression in a previous jet-cloud impact experiment but the compression scaling was not explored in detail.

This paper reports experimental results from the Caltech jet-cloud impact experiment together with comparison of the observed temperature and density increase with predictions based on the equation of state. In order to accomplish this investigation, comprehensive measurements of plasma parameters were performed using a Thomson scattering (TS) diagnostic, a fast imaging camera, a translatable laser interferometer, a monochromator, a visible-light photodiode, and a magnetic probe array. The time dependence of the temperature indicated existence of a significant radiative loss mechanism and so implies a minimum speed requirement for compression and heating to be successful. This paper is organized as follows. Section II describes the experimental setup

[a]Electronic mail: bhseo@caltech.edu
[b]Electronic mail: pbellan@caltech.edu

and diagnostics. Section III presents the experimental results. Section IV discusses (Sec. IV A) the jet-cloud penetration, the dynamic, thermal, and magnetic pressures, and (Sec. IV B) adiabatic heating, (Sec. IV C) the results showing that radiative losses are important in the experiment, (Sec. IV D) the relation of the results to MTF, and (Sec. IV E) shocks. Section V provides the conclusion.

II. EXPERIMENTAL SETUP

A. Vacuum chamber, jet formation, and collision with a gas cloud

The setup for the jet impact experiment is shown in Fig. 1. As seen in this figure, the 1.4 m diameter, 1.6 m long cylindrical vacuum chamber is much larger than the plasma dimensions so plasma interactions with the surrounding wall are negligible.[9–11] The jet is launched using coplanar, concentric copper electrodes consisting of a 20 cm diameter inner disk and a 50 cm diameter outer annulus. A cylindrical coordinate system $\{r, \theta, z\}$ is used with the axis defined by the vacuum chamber and the position of the coplanar electrodes defining $z = 0$. A bias coil located immediately behind the disk electrode generates an initial dipole-like poloidal magnetic field that links the inner and outer electrodes. A controlled amount of neutral hydrogen is puffed into the chamber from eight gas nozzles on the disk and eight gas nozzles on the annulus. High voltage from an electronically switched capacitor bank breaks down this hydrogen neutral gas to form plasma. Eight plasma loops are initially formed where each follows the initial dipole poloidal magnetic field. The inner parts of these loops mutually attract and merge to form the jet. The jet propagates in the z direction away from the electrodes and self-collimates via MHD forces.[13]

At a prescribed time slightly prior to the jet formation described above, a controlled amount of neutral argon gas is puffed into the vacuum chamber at $z \simeq 370$ mm by a 6 mm tube pointing towards the electrodes. The density of this argon gas cloud is measured by a fast ion gauge located 280 mm from the electrodes and the nominal neutral cloud density is $\simeq 2 \times 10^{20}$ m^{-3}. The location where the jet collides with the neutral cloud can be controlled by changing the time at which the argon is puffed and is set to be $z \simeq 280$ mm for diagnostic purposes. The argon cloud can be considered stationary relative to the jet because the jet velocity is $\simeq$70 km/s whereas the argon cloud moves at only a room-temperature thermal velocity (i.e., about 0.25 km/s). The jet and its associated magnetic field are compressed upon impacting with the argon cloud. The increase in density, temperature, and magnetic field resulting from the compression are measured and compared to models.

B. Diagnostics

Plasma parameters were determined using the diagnostics listed below:

1. A **fast imaging camera** (Imacon 200) takes 14 pictures with 0.5 μs interframe time and 10–30 ns exposure time; this camera views the plasma through a window on the side of the vacuum chamber.
2. A **Thomson scattering system** measures both electron temperature and density at the $z \simeq 280$ mm collision location. In a parameter regime where electron density $n_e = 10^{21}$–10^{23} m^{-3} and electron temperature $T_e = 2$–5 eV, both collective and non-collective Thomson scattering can occur depending on the scattering parameter, $\alpha \equiv 1/(k\lambda_D)$. Here, $k = |\mathbf{k}_s - \mathbf{k}_i|$, where $\mathbf{k}_s$ is the wave

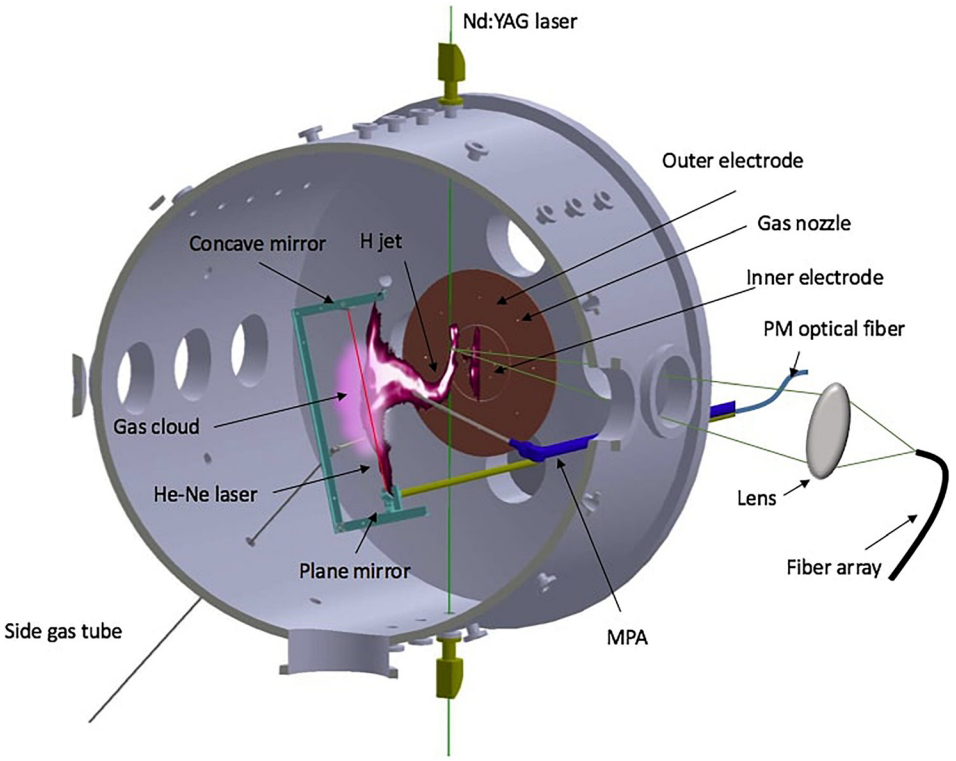

FIG. 1. Schematic of the experimental setup. PM optical fiber: polarization-maintained single mode optical fiber and MPA: magnetic probe array.

vector of the scattered signal, $\mathbf{k}_i$ is the wave vector of the incident laser beam, and λ_D is the plasma Debye length.[14] A second harmonic Nd:YAG laser was used with 532 nm center wavelength, 7 ns pulse width, 200 mJ pulse energy, and 10 Hz repetition rate. The plasma experiment was synchronized to the laser so that a laser pulse occurred at a controlled time relative to the starting time of the jet. A 50 mm focal length lens coupled the Thomson scattered light to a fiber array which transported this light to a 220 mm focal length spectrometer the output of which was imaged by a gated intensified CCD (ICCD) camera with 10 ns gate width to match the laser pulse width. The fiber array had 34 fibers (each 200 μm core size with 0.12 numerical aperture to match the spectrometer). The Thomson signal thus is a single-pulse measurement at a specific time in the plasma shot. Vertical binning was applied to the ICCD to obtain a high signal-to-noise ratio, so that spatial averaging was over ~40 mm in the direction of the laser beam (i.e., vertical direction in Fig. 1).

3. A **translatable, fiber-coupled, heterodyne interferometer**[15] measures the line-integrated density and jet velocity. The essential feature of this interferometer is a polarization-maintaining single-mode optical fiber installed in a 19 mm stainless steel tube. This tube enters the vacuum chamber through a vacuum feedthrough as shown in Fig. 1 and is both axially translatable and rotatable; only axial displacements were used in this work. Light from the fiber reflects from a 45° mirror, passes through the plasma, reflects from another mirror back through the plasma, reenters the fiber, and finally travels back to an optical table containing the remaining interferometer components (beamsplitter, detector, and laser). The interferometer measures a line-integrated electron density n_e and so the density measured by the interferometer is less than the peak density. The translatable interferometer can measure not only an axial profile of the line-integrated density but by taking into account the time dependence, can also determine velocity changes along the jet path.
4. A $f = 220$ mm **monochromator** measures the natural line emission radiated from the plasma. The radiated light is collected by a collimator that couples light to a multimode 100 μm core optical fiber that transports the light to the monochromator. Natural line emission is also measured by a photodiode with sensitivity absolutely calibrated in the 350–1000 nm range. The photodiode is coupled to the plasma via a multimode fiber with no collimator.
5. A translatable 60-coil **magnetic probe array** measures vector components of the magnetic field at 20 different locations spaced every 2 cm along the probe. By axially translating this array, a two-dimensional spatial profile of the **B** field is measured.[16]

III. RESULTS

A. Visible light images

Evidence of jet-cloud collision is provided by the fast imaging camera as shown in Fig. 2. The collision occurs at 7–8 μs after plasma breakdown. The bright visible emission during the collision is dominantly from neutral hydrogen atomic line radiation.

B. Line-integrated electron density measured by a translatable interferometer

The line-integrated electron density was measured by the interferometer as a function of both axial location and time. The space-time dependence of the line-integrated density provides a measurement of the jet axial velocity.[15] Figure 3 shows a plot of distance versus time (a) for a jet colliding with a target cloud and (b) for a jet-only situation (i.e., no target cloud). It is seen that at $z \simeq 280$ mm, a collision occurs as manifested by an abrupt deceleration of the jet and an increase in density (calibration in side color bar). Since the slope of the distance versus time plot in Fig. 3 corresponds to the jet velocity, peak densities from space-time plots were used to calculate the jet velocity. The change in

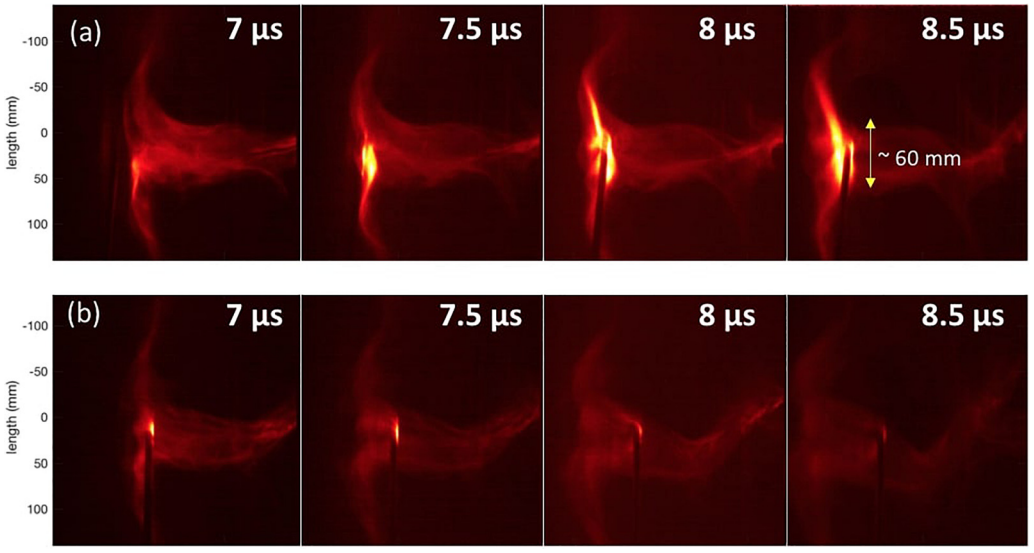

FIG. 2. False colored images taken by the fast movie camera with 0.5 μs interframe time from 7 μs (a) for a collision and (b) for a jet-only. The MPA can be seen in the image. The vertical axis is absolutely calibrated.

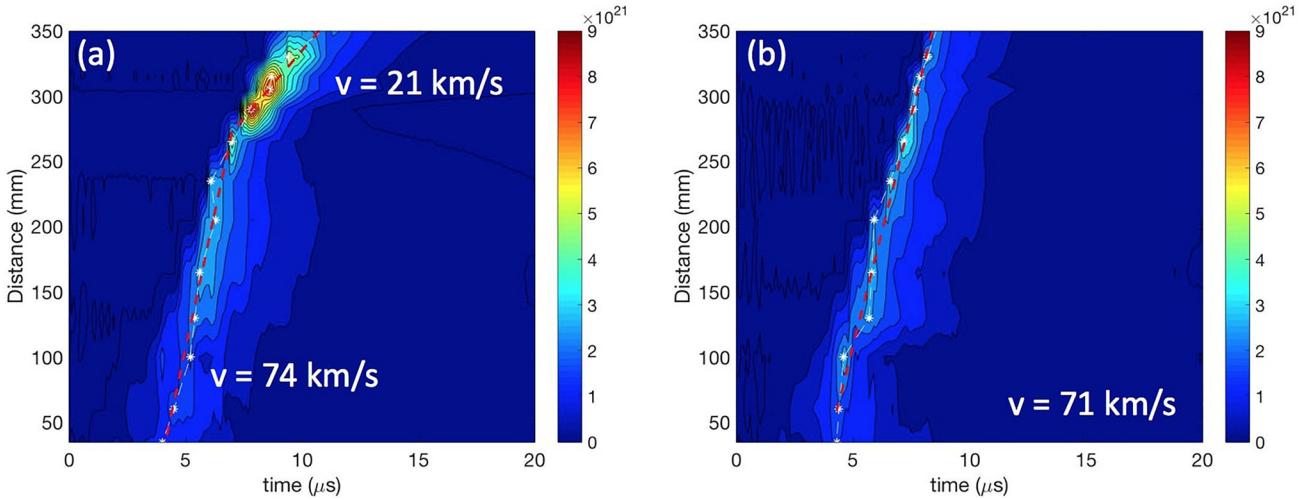

FIG. 3. Line-integrated electron density (in m^{-3}) measured by the interferometer (a) in a collision and (b) in a jet-only. The asterisks indicate the maximum densities at each location and the red dashed line is fitted using a linear function.

slope indicates a decrease in velocity from ∼70 km/s to ∼20 km/s at $z \simeq 280$ mm, where the jet impacts the target gas in contrast to the jet-only case which has no velocity decrease.

C. Thomson scattering

If the compression is adiabatic, the temperature should increase. The purpose of the Thomson scattering system is to determine this increase. Because of the high collisionality, it is assumed that electrons and ions are in thermal equilibrium with each other so the electron temperature measurement should also give the ion temperature. The Thomson scattering system measures the changes in both density and temperature during the compression. The density measured by the Thomson scattering is greater than that measured by the interferometer by a factor of about 10 because the interferometer measures a line-integrated electron density whereas the Thomson scattering measures a local electron density. Samples of the measured Thomson scattering spectrum are shown in Fig. 4. As mentioned above, the spectrum of the scattered laser radiation depends on α. For $\alpha > 1$ as shown in Fig. 4(a), the spectrum has a pair of peaks offset at ±5 nm from the laser line and the separation of these peaks corresponds to the electron density. The baseline of this spectrum is determined by continuum radiation which scales as n_e^2 and so at very high density where the continuum radiation becomes large, the baseline rises and so reduces the signal-to-noise ratio.

The absolute value of the electron density is conventionally determined using Rayleigh or Raman scattering to calibrate the sensitivity of a Thomson scattering system.[14,17,18] However, setting up for Rayleigh or Raman scattering is cumbersome because this calibration requires filling the large vacuum chamber with several hundred mTorr of neutral gas. In the $\alpha > 1$ regime, an alternative, simpler method to determine the absolute electron density can be used as described in the following three paragraphs.

The Thomson scattering spectral density function is expressed as[14]

$$S(\mathbf{k},\omega) = \frac{2\pi}{k}\left|1 - \frac{\chi_e}{\epsilon}\right|^2 f_{eo}\left(\frac{\omega}{k}\right) + \frac{2\pi Z}{k}\left|\frac{\chi_i}{\epsilon}\right|^2 f_{io}\left(\frac{\omega}{k}\right), \quad (1)$$

where $\varepsilon = 1 + \chi_e + \chi_i$ is the dielectric function, χ_e is the electron susceptibility, χ_i is the ion susceptibility, Z is the averaged ionization state, $\omega = \omega_s - \omega_i$ where ω_s is the

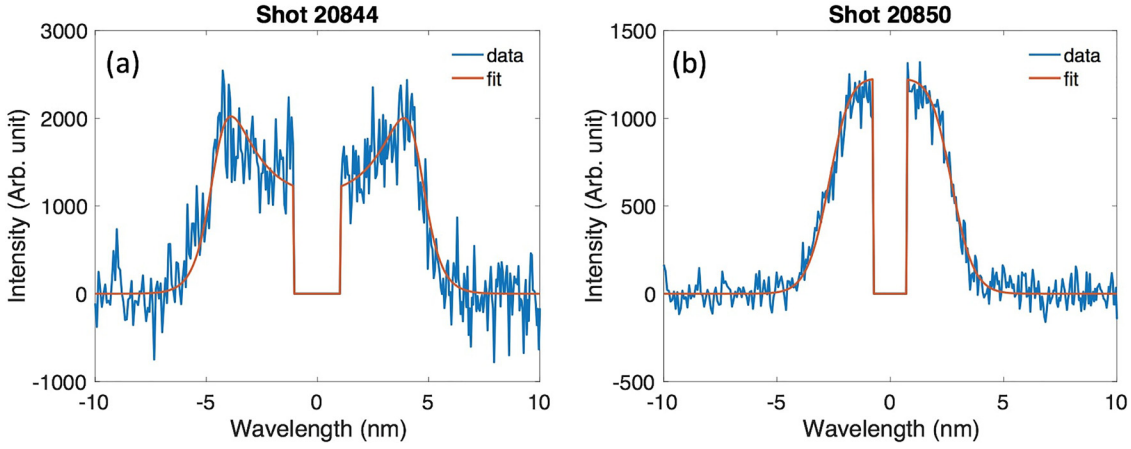

FIG. 4. Samples of the measured TS spectra. (a) $n_e = 9 \times 10^{22}$ m^{-3}, $T_e = 3.4$ eV, and $\alpha = 1.3$ and (b) $n_e = 1.5 \times 10^{22}$ m^{-3}, $T_e = 1.9$ eV, and $\alpha = 0.7$.

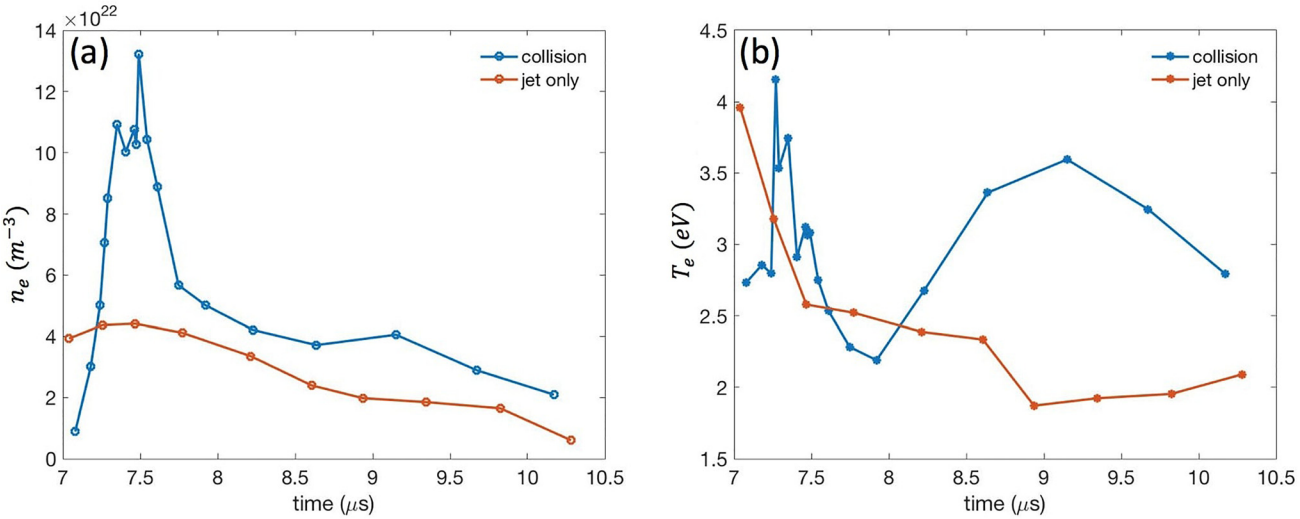

FIG. 5. Time dependence of (a) electron density and (b) temperature measured by TS in a collision (blue) and in a jet-only (red).

scattered frequency and ω_i is the incident laser frequency, and $f_{eo}(\omega/k)$ and $f_{io}(\omega/k)$ are, respectively, the electron and ion velocity distribution functions. Because of the high collisionality, both electrons and ions were assumed to have a Maxwellian velocity distribution function. The second term in the RHS of Eq. (1) was neglected because this term represents the ion contribution which, while observable, cannot be resolved by the spectrometer being used.

Since χ_e and χ_i are functions of α^2, both χ_e and χ_i are negligible in the regime where $\alpha \ll 1$. In this case $S(\mathbf{k}, \omega)$ has the same profile as $f_{eo}(\omega/k)$ and this situation is called non-collective Thomson scattering. However, in the regime where $\alpha > 1$, the spectrum depends on χ_e and χ_i and this situation is called collective Thomson scattering. The $\alpha > 1$ condition is related to the propagation behavior of the electron plasma wave (also called the Bohm-Gross or Langmuir wave). The finite χ_e and χ_i contributions become significant if $\varepsilon \to 0$ which happens when $\omega = \omega_{pe}$, where ω_{pe} is the electron plasma frequency; this gives the twin peaks in Fig. 4(a). Since ω_{pe} is a function of n_e, the electron density can be obtained from the offset of these peaks from the laser frequency. Since α is also a function of electron temperature, the electron temperature can be obtained by fitting a spectral density function to the data.

However, the twin-peak feature is unclear if $\alpha < 1$ but α is not negligible; this situation leads to increased error in the density measurement. Thus, we first obtained a relative density by integrating a spectrum and then an absolute calibration was performed using a spectrum for which the twin-peak feature is clearly observed as in Fig. 4(a). Thus, a spectrum having $\alpha > 1$ is used to provide calibration for both $\alpha < 1$ and $\alpha > 1$ situations because the Thomson scattering signal intensity is linear in density.

Figure 5 shows the electron density and temperature time dependence measured by the Thomson scattering system. Each data point was measured from a separate shot with identical external parameters except that the measurement was made at a different time. These measurements indicate that the density increases by a factor of ~2.5 for a jet-target collision compared to the situation of no collision (i.e., jet-only). However, as shown in Fig. 6, the temperature has a more complicated time dependence: the temperature first increases and then quickly decreases.

D. Magnetic probe array

Since the Lundquist number ($S = Lv_A/\eta$, where L is the typical length scale of the system, η is the magnetic diffusivity and v_A is the Alfvén velocity) in this experiment is about 72, we can treat the plasma as being in the ideal MHD regime. In the ideal MHD magnetic flux is frozen into the plasma frame so the magnetic field should also be compressed during the plasma compression.[11] The magnetic probe array was used to measure the magnetic field embedded in the plasma jet. Figure 7 shows the measured magnetic field at 7.9 μs for (a) the jet colliding with a target cloud and (b) the jet-only situation (no collision). Colored contours in this figure indicate the toroidal field, black lines indicate poloidal flux surfaces, and arrows indicate the poloidal field. It is seen that B_r and B_ϕ increase in a collision whereas B_z hardly changes. Figure 8 shows the ratio of the field when

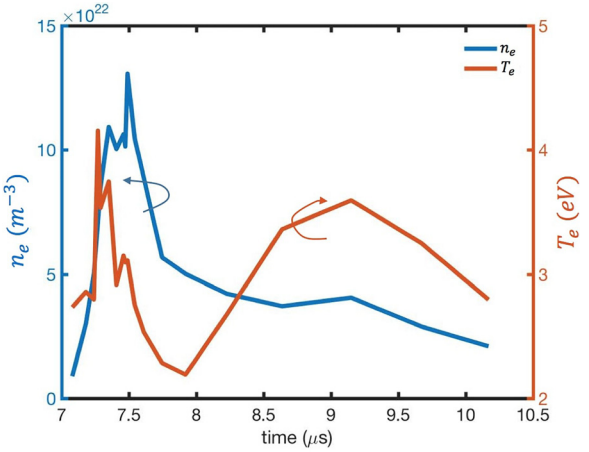

FIG. 6. Time dependence of the electron density and temperature in a collision.

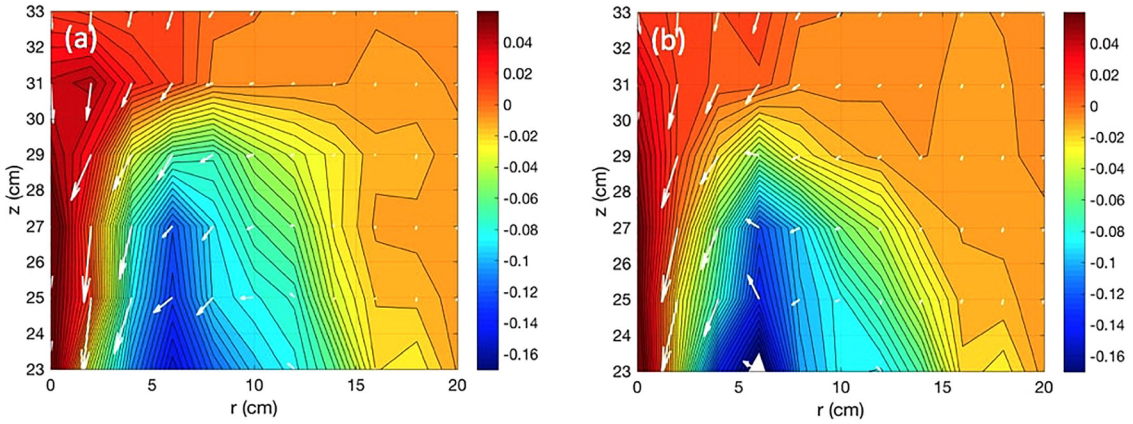

FIG. 7. Magnetic field (a) in a collision and (b) in a jet-only. The color contour indicates the toroidal field and the arrows indicate the poloidal field. The unit of the contour is in Tesla.

the jet collides with a target cloud denoted as $|B_{\text{collision}}|$ to the field when there is no collision denoted as $|B_{\text{jet}}|$; at $r = 12$ cm and $z = 29$ cm, $|B_{r,\text{jet}}| \simeq 0.012$ T, $|B_{r,\text{collision}}| \simeq 0.016$ T, $|B_{\theta,\text{jet}}| \simeq 0.008$ T, $|B_{\theta,\text{collision}}| \simeq 0.032$ T, $|B_{z,\text{jet}}| \simeq 0.006$ T, $|B_{z,\text{collision}}| \simeq 0.003$ T, $|B_{\text{jet}}| \simeq 0.016$ T, and $|B_{\text{collision}}| \simeq 0.037$ T. This figure shows that the magnetic field is compressed by more than a factor of 2.2 which is consistent with the electron density increase. The magnetic field compression region is off-axis because this region is where B_r and B_ϕ are dominant components.

IV. DISCUSSION

A. Jet-cloud interpenetration and dynamic, magnetic and thermal pressures

The argon gas cloud is presumed to be effectively acting as a compressing liner from the point of view of an observer in the jet frame. In order to validate the presumption, it is necessary to estimate how much the jet penetrates the gas cloud. The penetration depth can be estimated by calculating the mean free path for a hydrogen ion penetrating the argon neutral gas; this is the jet penetration length. The mean free path is

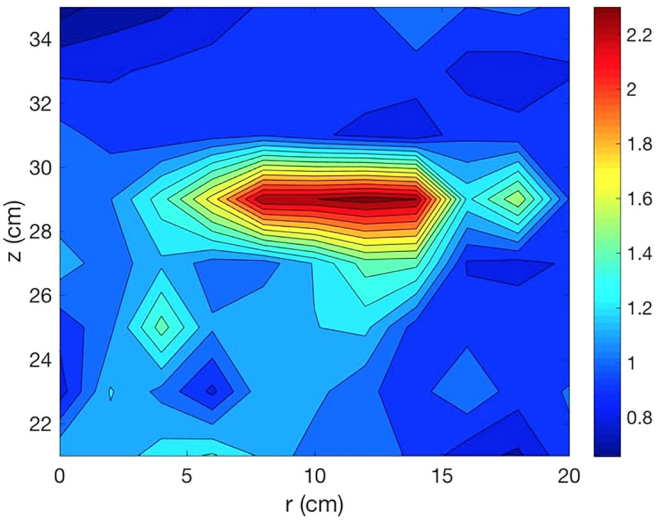

FIG. 8. Ratio of $|B_{collision}|$ *to* $|B_{jet}|$.

$$l_{mpf} = \frac{v_{rel}}{\nu_{in}} = \frac{v_{rel}}{n_{Ar} K_{in}} = \frac{v_{rel}}{n_{Ar} v_{rel} \sigma_{in}} = \frac{1}{n_{Ar} \sigma_{in}}. \quad (2)$$

Here, the relative jet velocity v_{rel} (70 km/s corresponding to 25 eV) is used instead of the ion thermal velocity ($v_{i,th} \simeq 22$ km/s), since $v_{rel} > v_{i,th}$. ν_{in} is the hydrogen ion-argon neutral momentum transfer collision frequency, n_{Ar} is the argon gas cloud density, and $K_{in} = v_{rel}\sigma_{in}$ is the hydrogen ion-argon neutral atom momentum transfer collision rate coefficient, where σ_{in} is the hydrogen ion-argon neutral atom momentum transfer collision cross-section. The average for K_{in} in velocity space is not taken because v_{rel} is used instead of $v_{i,th}$ so that v_{rel} is canceled out. Using $n_{Ar} = 2 \times 10^{14}$ cm^{-3} and $\sigma_{in}(25\,\text{eV}) = 1.9 \times 10^{-16}$ cm^2 (Ref. 19) gives $l_{mfp} \simeq 26$ cm. This mean free path is not consistent with what actually happens in the experiment because the velocity decrease indicates that the jet interacts with the gas cloud within a few cm as shown in Fig. 3.

Instead, since the jet velocity quickly drops to 20 km/s (corresponding to 2 eV), using $\sigma_{in}(2\,\text{eV}) = 2.8 \times 10^{-15}$ cm^2 (Ref. 19) would give $l_{mfp} \simeq 2$ cm. In addition, although the argon gas density was measured using a spatially localized home-made fast ion gauge, uncertainties could exist in the argon gas cloud density which could result in a low estimate for the gas density. Also, the argon neutral atom density is expected to increase during the compression so that the actual mean free path should decrease. Figure 4 of Moser and Bellan[11] has a configuration that is essentially identical to this experiment and shows a spatial separation of the argon and hydrogen spectra; this separation supports the conclusion that the argon cloud and the hydrogen jet have negligible interpenetration.

The dynamic pressure of the argon effective liner is also relevant in the experiment; dynamic pressure of the argon gas cloud is $P_D = \rho v_{rel}^2$ where $\rho = n_{Ar} m_{Ar}$, thermal pressure of the hydrogen jet is $P_{th} = nk_BT = (n_e + n_i)k_BT \simeq 2nk_BT$ and magnetic pressure of the hydrogen jet is $P_B = B^2/(2\mu_0)$. The observed quantities, $n \simeq n_e \simeq 4 \times 10^{22}$ m^{-3}, $T \simeq T_e \simeq 2.5$ eV, and $B \simeq 0.24$ T at the axis and the relative velocity v_{rel} of the gas cloud set to be the same as 70 km/s jet velocity give $P_D \simeq 6.6 \times 10^4$ Pa, $P_B \simeq 2.3 \times 10^4$ Pa, and $P_{th} \simeq 3.2 \times 10^4$ Pa. Thus, P_D exceeds $P_B + P_{th}$ corresponding to the existence of a dynamical compression.

B. Adiabatic heating

Since adiabatic heating is expected during the compression, the plasma density and temperature are expected to increase as $P \sim n^{\gamma}$, $T \sim n^{\gamma-1}$, where $\gamma = (N+2)/N$ is the adiabatic constant and N is the number of degrees of freedom. In choosing the appropriate value of N to determine γ for a plasma that is collisional and adiabatic, it is necessary to realize that compression in one or two spatial dimensions will have the same γ as compression in all three spatial dimensions because collisions will equipartition the kinetic energy of a particle among the three degrees of freedom of the motion;[20] i.e., collisions will make $N = 3$ and $\gamma = 5/3$ even if the compression involves only one or two spatial dimensions. Also, the collisionality in this situation is invariant with adiabatic compression because the collision frequency of electrons or ions is proportional to $\sim nT^{-3/2}$ where n is the electron or ion density and T is the electron or ion temperature and for $\gamma = 5/3$, the adiabatic relation gives $n \sim T^{3/2}$. Thus, $nT^{-3/2}$ in the collision frequency is constant resulting in an invariant collision frequency for the adiabatic compression. Due to high collisionality, the adiabatic invariant μ is not conserved because of the transfer of a portion of the perpendicular temperature ($T_{\perp}$) to the parallel temperature ($T_{\parallel}$) so as to have $T_{\perp} = T_{\parallel}$.

The increase of $n = 4 \times 10^{22}$ m^{-3} to $n = 10^{23}$ m^{-3} indicates the observed compression ratio is a factor of 2.5 as shown in Sec. III C. Using $\gamma = 5/3$ gives $T_f \sim T_i (n_f/n_i)^{2/3}$, where i and f indicate initial and final, respectively. Thus, a 2.5 eV initial temperature should increase to 4.6 eV.

Although γ results from adiabatic compression with three degrees of freedom, the compression ratio is provided by the geometrical dimension of the compression. Since the Caltech experiment involves a linear compression, we assume that the geometrical dimension is one-dimensional, so the flux conservation $Br^2 = const.$ reduces to $Bl = const.$, where l is the axial length being compressed. This gives $B \sim n$ since $n \sim 1/l$. Thus, the magnetic field should increase by a factor of 2.5 which is consistent with the experimental observations.

While the changes in density, magnetic field, and velocity were consistent with the expectations, the temperature had a rather complicated time-dependence that differed from the expectations. The temperature increases at first but then declines very quickly suggesting the development of a rapid loss mechanism.

C. Radiative loss

The increase in energy density as a result of the compression is $\Delta E_c \equiv \Delta(n_e \kappa_B T_e) \simeq 57$ mJ/cm^3, where κ_B is Boltzmann's constant. If a loss mechanism is to explain the sudden temperature reduction noted at the end of Sec. III C, the loss mechanism must remove this ΔE_c in a time shorter than the compression time. Conduction loss is suspected to be weak or negligible because the large machine size minimizes plasma interactions with the wall. However, radiative loss could be associated with the temperature decline. Possible radiative loss mechanisms are continuum radiation and line emission which will now be discussed.

1. Continuum radiation

Continuum radiation can be important in high-density plasmas and results from both radiative recombination and Bremsstrahlung radiation.[21–23] In the experimental regimes where the temperature is less than 5 eV, radiative recombination dominates Bremsstrahlung.[23] The baseline of the Thomson scattering spectrum corresponds to the continuum radiation. The time dependence of the continuum radiation as determined from this baseline is shown in Fig. 9 and is compared with the continuum radiation calculated with the theory in Ref. 23 using the electron density and temperature measured by Thomson scattering. It is seen that the calculated continuum radiation is in good agreement with the measured continuum radiation.

The characteristic time for energy density ΔE_c to be lost by some mechanism is related to the loss power density p for that mechanism by $\tau = \Delta E_c/p$. Figure 9 shows that the continuum radiation power peaks at 4.5×10^9 W m^{-3} and so the time for continuum radiation to radiate the energy increase resulting from compression is $(5.7 \times 10^4$ J m$^{-3})/(4.5 \times 10^9$ W m$^{-3}) \simeq 13$ μs which is an order of magnitude longer than the observed temperature decay time of <1 μs seen in Fig. 6. Thus, although there clearly is an increase in the continuum radiation, quantitative estimates of the power loss by continuum radiation show that this power loss is inadequate to explain the observed loss of electron thermal energy and so additional loss mechanisms must be considered. However, in a fusion-grade MTF condition, the most dominant radiative loss is Bremsstrahlung continuum radiation.[4]

2. Line emission

Another possible radiative loss mechanism in this experiment is line emission by some combination of hydrogen atoms, argon atoms, and argon ions. Impurity line emission is observed to be negligible. Because a hydrogen ion is just a proton and so has no bound electrons, a fully ionized hydrogen plasma jet should emit no line radiation because line radiation involves a change in the energy state of bound electrons. However, if plasma electrons and ions *combine* to create neutral atoms, line emission could become large. In a very high-density plasma, such as the experiment discussed here, two possible recombination mechanisms exist. The first is radiative recombination and the second is three-body

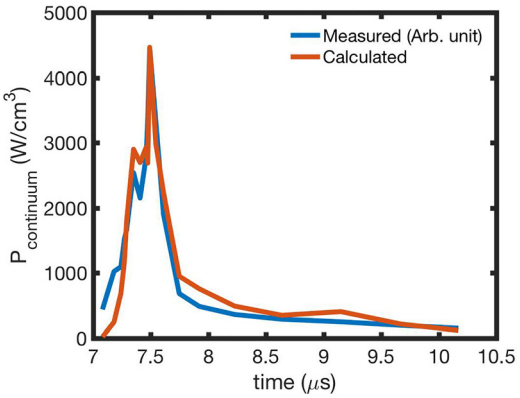

FIG. 9. Measured (blue) and calculated (red) continuum radiation intensity in a collision. Note that the measured continuum radiation intensity is in arbitrary units and normalized to the calculated intensity.

recombination, the inverse process of ionization. The radiative recombination rate coefficient can be expressed as[24,25]

$$K_R = 2.7 \times 10^{-13} T_e^{-3/4}\ \mathrm{cm^3 s^{-1}} \tag{3}$$

and the three-body recombination rate coefficient can be expressed as

$$K_c = 5.6 \times 10^{-27} T_e^{-9/2} n_e\ \mathrm{cm^3 s^{-1}}. \tag{4}$$

In the density and temperature regime of the experiment discussed here ($n_e = 1 \times 10^{23}\ \mathrm{m^{-3}}$, $T_e < 5\,\mathrm{eV}$), the three-body recombination rate is much greater than the radiative recombination rate.

The other possible mechanisms for creating neutral hydrogen atoms are the hydrogen ion-hydrogen atom charge-exchange and the hydrogen ion-argon atom charge-exchange. The charge-exchange rate coefficient between a hydrogen ion and a hydrogen neutral atom is much greater than the three-body recombination rate coefficient; the cross-section $\sigma_{cx}(25\,\mathrm{eV}) \simeq 2.0 \times 10^{-15}\,\mathrm{cm^{-2}}$ (Ref. 19) gives $K_{\mathrm{cx}} = \sigma_{cx} v_{jet} \simeq 2 \times 10^{-8}$. However, we believe that the jet is initially fully ionized so there are initially negligible hydrogen atoms in the jet so charge-exchange with neutrals cannot occur. In the case of the hydrogen ion-argon atom charge-exchange, using the hydrogen ion-argon atom charge-exchange cross-section $\sigma_{\mathrm{cx}}(25\,\mathrm{eV}) \simeq 1 \times 10^{-19}\,\mathrm{cm^{-2}}$ (Ref. 26) gives the rate coefficient $K_{\mathrm{cx}} = \sigma_{\mathrm{cx}} v_{jet} \simeq 7 \times 10^{-13}\,\mathrm{cm^{-3}/s}$ from which we have the rate $\nu_{\mathrm{cx}} = n_{Ar} K_{\mathrm{cx}} \simeq 140\,\mathrm{s^{-1}}$, where $n_{\mathrm{Ar}} \simeq 2 \times 10^{14}\,\mathrm{cm^{-3}}$; we should note that the cross-section at 25 eV in Ref. 26 is an extrapolated value from the cross-sections at higher energies. For the three-body recombination rate, Eq. (4) gives $K_c(n_e = 4 \times 10^{16}\,\mathrm{cm^{-3}}, T_e = 2.5\,\mathrm{eV}) \simeq 3.6 \times 10^{-12}\,\mathrm{cm^{-3}/s}$ from which we have the rate $\nu_c = n_e K_c \simeq 1.4 \times 10^5\ \mathrm{s^{-1}}$. Thus, the three-body recombination dominates the charge-exchange.

Figure 10(a) shows the time-dependent line emission of the hydrogen Balmer alpha line (H_α, 656 nm) measured by a monochromator. It is seen that the H_α emission suddenly increases at 7–8 μs which is when the jet collides with the gas cloud suggesting that three-body recombination could be a radiative loss mechanism.

The power in visible light emission such as the H_α line is much less than that emitted in the deep ultraviolet (UV) of the Lyman series but measurement of deep UV emission requires special in-vacuum detectors since UV is blocked by windows. The UV radiative power can be inferred from the Balmer lines using the relation $P_{ij} = A_{ij} N_i \Delta E_{ij} \mathrm{x}$, where A_{ij} is the spontaneous radiation coefficient from the principle quantum level i to the principle quantum level j, where $i > j$, N_i is the population density of the level i, and ΔE_{ij} is the energy difference between the levels i and j. The coefficients A_{ij} and ΔE_{ij} are well established for hydrogen. Since the Lyman β line and the Balmer α line result from the same $n = 3$ energy level, we obtain $P_{L,\beta} \approx 8.15 P_{B,\alpha}$, where $P_{L,\beta}$ is the radiative power of the Lyman β line and $P_{B,\alpha}$ is that of the Balmer α line.[27]

Figure 10(b) shows the time-dependent visible emission measured by a photodiode; the UV radiative power is inferred from this measurement. Light was coupled to the photodiode by a multimode optical fiber with no collimator. For this measurement, the diode responsivity was $\varepsilon = 0.345\,\mathrm{A/W}$ at 656 nm (Ref. 28) so $P_{pd} = V_{pd}/(\varepsilon R)$ where P_{pd} is the light power in watts illuminating the photodiode and V_{pd} is the photodiode voltage across an $R = 50\,\Omega$ load resistor. The radiated plasma line emission power P_{line} was determined from the power incident onto the photodiode by the relation $P_{line} = P_{pd} \times (4\pi r^2/A_{fiber}) \times 1/T_f \times 1/T_w$, where $r = 0.95$ m is the distance from the optical fiber to the plasma center, $A_{fiber} = 1.26 \times 10^{-7}\ \mathrm{m^2}$ is the area of the 400 μm diameter fiber, and $T_f \sim 0.86$ is the transmittance of the optical fiber. T_w, the transmittance of the chamber window, was assumed to be 0.9.

The optical fiber transmittance T_f was determined as follows: the intensity of a light bulb was measured by the photodiode both through the fiber and directly without the fiber and the intensity ratio was 0.0085. Since the fiber area is $1.26 \times 10^{-7}\ \mathrm{m^2}$ and the photodiode area is $1.3 \times 10^{-5}\ \mathrm{m^2}$, the ratio of the areas is 0.0098. Thus, transmittance of the fiber including the coupling efficiency of the light to the fiber is 0.0085/0.0098 = 0.86.

If it is assumed that all the radiation comes from the Balmer α line and that the plasma is optically thin, then $P_{L,\beta} \simeq 8.15 P_{line}$. This assumption is reasonable because the photodiode is sensitive from 350 nm to 1100 nm, only Balmer series are in this wavelength range, Balmer α has the largest emissivity in the Balmer series, and Argon emission is negligible compared to Balmer α emission as observed using the monochromator. Combining these relations gives the power radiated in Lyman β as

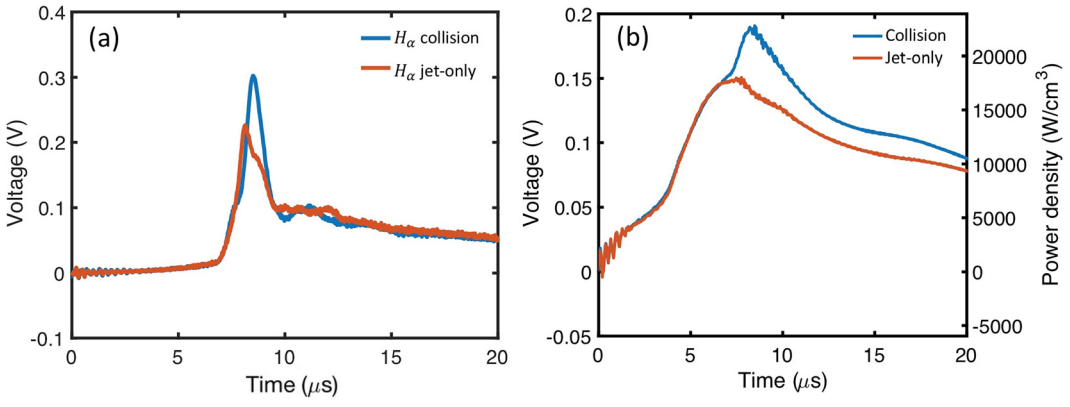

FIG. 10. (a) H_α emission intensity measured by the monochromator and (b) visible-light emission intensity measured by the photodiode in a collision (blue) and in a jet-only (red).

$$P_{L,\beta} = 8.15 \frac{4\pi r^2}{\varepsilon R T_f T_w A_{fiber}} V_{pd}\,\mathrm{W}. \quad (5)$$

In order to compare this prediction to the experiment, the volume of the radiating compressed plasma region is required. Using the photo image in Fig. 2 and the TS measurement, this region is estimated to be a cylinder having 30 mm radius (vertical direction in Fig. 2) and 20 mm length (horizontal direction in Fig. 2) in which case the volume of the radiating region is 5.7×10^{-5} m^3. The 30 mm cylinder radius estimated from the photos is consistent with the 40 mm extent of the TS measurement so the radius estimate corresponds to the radial extent of the highest density region. The cylinder axial length is estimated from the jet slowing down to 20 km/s and so moving 20 mm in 1 μs. The power density of the Lyman α radiation is then related to the photo-diode voltage by

$$p_{L,\beta} = 1.4 \times 10^5 \frac{4\pi r^2}{\varepsilon R T A_{fiber}} V_{pd}\,\mathrm{W\,m^{-3}}. \quad (6)$$

This gives the radiated power per cubic meter. From this measurement, $\Delta E_c(J/\mathrm{cm}^3)/p_{L,\beta}(W/\mathrm{cm}^3) \simeq 1.2\,\mu$s was obtained which is of the order of the observed temperature decrease. Moreover, the radiative power of Lyman α, $p_{L,\alpha}$, is known to be greater than $p_{L,\beta}$ so the radiative recombination UV line emission is likely the dominant radiative loss responsible for the observed temperature decrease.

Using the measured power density, the Einstein spontaneous emission coefficient A_{ij} and the energy difference ΔE_{ij} of the ground state to $n=3$ state of hydrogen, the population density of the $n=3$ state can be calculated to be

$$n_3 = \frac{P_{B,\alpha}}{A_{2,3}\Delta E_{2,3}} \simeq 1.8 \times 10^{15}\,\mathrm{cm^{-3}}. \quad (7)$$

From the inferred n_3, we could roughly infer the ground state neutral density n_1 if we assume a Boltzmann equilibrium relates the ground state to the $n=3$ state, i.e.,

$$\frac{n_3}{n_1} = \frac{g_3}{g_1}\exp(-(E_3 - E_1)/k_B T_e) \simeq 0.45, \quad (8)$$

so

$$n_1 = n_3/0.45 \simeq 4 \times 10^{15}\,\mathrm{cm^{-3}}, \quad (9)$$

where $T_e = 4$ eV, $g_1 = 2$, and $g_3 = 18$ are the respective statistical weights of the ground state and the $n=3$ state. This neutral density is created by three-body recombination. Using Eq. (4) with $n_e = n_i = 4 \times 10^{16}\,\mathrm{cm^{-3}}$ and $T_e = 2.5$ eV gives the neural atom density creation rate to be $dn_n/dt = K_c n_e n_i = 5.6 \times 10^{-27}(n_e T_e^{3/2})^3 = 5.8 \times 10^{21}\,\mathrm{cm^{-3}\,s^{-1}}$. Thus, in one microsecond, the amount of neutral density created is 5.8×10^{15} cm^{-3} which is consistent with the experimentally obtained neutral density in Eq. (9). Also, the neutral atom creation rate is invariant with adiabatic compression since $n_e T_e^{3/2}$ is constant for 3D adiabatic compression. This implies that preheating is required to prevent radiation by three-body recombined neutral atoms. From this estimate, the ratio of the neutral density to the electron density is 0.04.

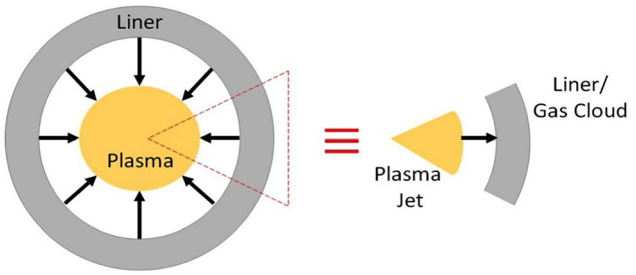

FIG. 11. LHS represents the compression process in a MTF while RHS shows the same process with a reversed reference frame. Note that the geometrical dimensionality of MTF is cylindrical while that of the Caltech experiment is linear.

D. Criterion of compression time relevant to MTF

The compression investigation reported here is relevant to MTF due to the following reasons. As shown in Fig. 11, the situation of the jet-cloud collision experiment is equivalent to MTF; all that has happened is a change of frames. The number of degrees of freedom is $N=3$ not only in the Caltech experiment reported here but also for actual MTF due to the collision frequency being invariant in adiabatic compression with $N=3$ as was argued in Sec. IV B. The geometrical dimensionality of MTF is cylindrical while the Caltech experiment is linear; this would be different in compression ratio but would give the same compression physics in terms of the density, temperature, and magnetic field of the collisional adiabatic compression. As discussed in Sec. IV C, radiative loss suppresses the temperature increase in the Caltech experiment. This motivates calculation of a criterion for the compression time to outrun radiative loss in a fusion-relevant context; this will now be discussed.

The radiative loss mechanism depends on the temperature. If the temperature is a few eV, line emission by neutral atoms created by three-body recombination is dominant as found here, but if the temperature is a few keV as in a fusion-relevant context, Bremsstrahlung continuum radiation would be dominant. At each stage having a characteristic compression time τ_c, the compression time should be much less than the radiative time τ_R, i.e., it is necessary to have

$$\tau_R \simeq \frac{\Delta E_c(\mathrm{J/cm^3})}{(p_{line} + p_{continuum})(\mathrm{W/cm^3})} \gg \tau_c. \quad (10)$$

In a fusion-grade regime, P_{line} can be negligible because $\alpha_c/\alpha_R \simeq 2.1 \times 10^{-14} T_e^{-15/4} n_e \ll 1$ in the range $n_e < 1 \times 10^{23}$ cm^{-3} and $T_e > 1$ keV so three-body recombination rarely occurs. Continuum radiation by radiative recombination is also negligible because continuum radiation by Bremsstrahlung is much greater than by radiative recombination.

If P_{line} is neglected for fusion-grade temperatures and only Bremsstrahlung continuum radiation power (p_B) is considered,[23] Eq. (10) reduces to

$$\tau_R \simeq \frac{\Delta E_c}{p_B} \simeq \frac{\Delta(n_e T_e)}{1.58 \times 10^{-32} n_e^2 \sqrt{T_e}}. \quad (11)$$

If we assume the initial density and temperature to be relatively low compared to that of the final compressed state but not as low as in the Caltech experiment where line emission becomes important, τ_R becomes

$$\tau_R \simeq \frac{n_e T_e}{1.58 \times 10^{-32} n_e^2 \sqrt{T_e}}, \tag{12}$$

$$= \frac{\sqrt{T_e}}{1.58 \times 10^{-32} n_e}. \tag{13}$$

Thus, τ_c should be much less than τ_R so that radiation does not suppress the temperature increase.

Figure 12 plots τ_R as given by Eq. (13) for various MTF-relevant electron densities and temperatures and also indicates experimental results from selected experiments. The Lawson criterion, $n\tau_E = 10^{14}$ s/cm^3, where n is the density and the confinement time τ_E has been set to equal τ_R, is shown as a green line; the Lawson criterion is satisfied above this line (the green line does not imply that the temperature is 100 eV). For adiabatic compression to lead to fusion, the compression time must be shorter than the time given by the sloped line for each segment of the compression and the final result must be above the green line.

For the MagLIF experiment[5] shown in the upper right in Fig. 12, the initial condition shown as a green triangle is $n = 2 \times 10^{20}$ cm^{-3} (0.7 mg/cm^{-3} for D gas, 2 amu) and $T = 100$ eV. Since the initial target radius is 2.325 mm and the final radius is 62.5 μm, the radial compression ratio is ~1380. From the adiabatic relation, $T_f \sim T_i (n_f/n_i)^{2/3}$, the expected temperature is ~7 keV (shown as a blue circle in the MagLIF region) when $n = 1 \times 10^{23}$ cm^{-3} is achieved and τ_c is less than 7.1 ns. However, the compression time is presumed to be at least a few tens of nanoseconds (~33 ns inferred from 2.325 mm initial radius and 70 km/s velocity) so significant energy loss might occur from Bremsstrahlung radiation that suppresses the temperature increase; the reduced final temperature is shown as a red star. This provides a possible explanation for why 3 keV was achieved instead of 7 keV and suggests that a faster compression time would lead to higher final temperatures.

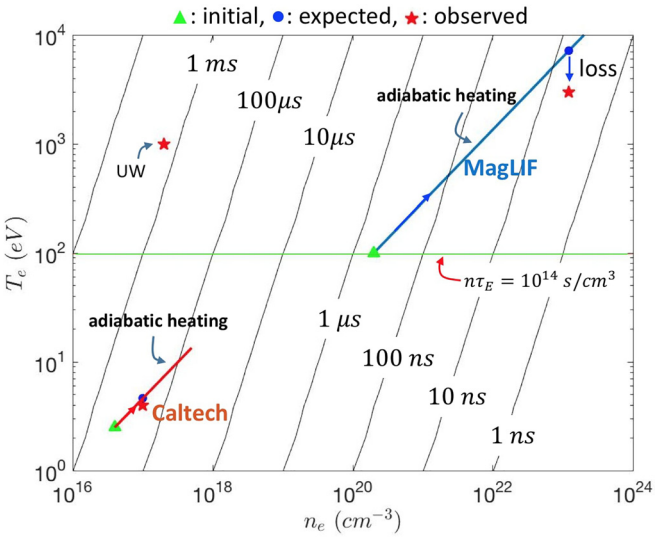

FIG. 12. Radiative time τ_R as a function of electron density and temperature for both small laboratory and fusion-grade experiments. The blue and red lines indicate the adiabatic heating ($T_f \sim T_i (n_f/n_i)^{2/3}$) of MagLIF[5] and Caltech experiments, respectively. The horizontal green line represents the Lawson criterion, $n\tau_E = 10^{14}$ s/cm^3. UW: University of Washington.

For the Z-pinch experiment at the University of Washington (UW),[29] the $\tau_R = 1.6$ ms is shown as a red star located at $n_e = 1 \times 10^{17}$ cm^{-3} and $T_e = 1$ keV in Fig. 12. Since the experiment duration is ~50 μs, the radiation time seems to be much longer than the required compression time. However, it should be noted that the temperature was inferred from the measured electron density using the pinch relation rather than from a direct measurement.

For the Caltech experiment shown in the bottom left in Fig. 12, the initial density is 4×10^{16} cm^{-3} and the initial temperature is 2.5 eV. Since the density was observed to increase to 1×10^{17} cm^{-3}, the linear compression ratio is about 2.5 so the temperature was expected to increase to 4.6 eV. As can be seen in Fig. 6, the temperature initially increased to ~4 eV which is consistent with the initial compression time being shorter than the radiation time (Bremsstrahlung or radiative recombination). However, the temperature quickly dropped as a result of radiative loss by line emission of three-body recombined neutral atoms.

The electron-electron collision frequency $\nu_{ee} = 4 \times 10^{-12} n \ln\Lambda / T^{3/2}$, where n is the density in m^{-3}, T is the temperature in eV, and $\ln\Lambda$ is the Coulomb logarithm, from which we obtain the initial collision time of MagLIF, $\tau_{ee} = 1/\nu_{ee} \simeq 0.2$ ps which is much shorter than the total compression time. Since the collision frequency is invariant in collisional adiabatic compression, the final collision time should be the same as the initial collision time but is shorter than 0.2 ps due to the lower temperature resulting from the radiative loss than an adiabatically compressed temperature. The collision time of the Caltech experiment is ~5 ps and that of UW is 7 ns so both these experiments are collisional. For the ion-ion collision, the collision time is longer by $\sqrt{m_i/m_e} \simeq 43$ for hydrogen but still remains in the collisional regime.

E. Shocks

In order for a shock to be launched, an object must move at a speed greater than the sound speed (or magnetosonic speed for a MHD shock). In our experimental configuration, we consider three situations as illustrated in Fig. 13; (a) a hydrodynamic (HD) shock forming in the argon gas cloud, (b) a parallel MHD shock forming in the hydrogen jet, and (c) a perpendicular MHD shock forming in the hydrogen jet. We should note that the parallel MHD shock is identical to the HD shock. In Fig. 13, the numbers 1 and 2, respectively, indicate unshocked and shocked regions. v_1 and v_2, respectively, are velocities in the shock frame. The shock jump conditions used here are derived in the shock frame.[30] The shock velocity in the lab frame is defined to be v_s, so adding v_s to the shock frame velocities gives lab frame velocities v_1' and v_2'; $v_1' = v_1 + v_s = 0$ and $v_2' = v_2 + v_s = v_2 - v_1 = v_p$, where v_p is a piston velocity of the piston-generated shock configuration in the lab frame and corresponds to v_{jet} in the experiment. Since the directions of flow in the shock frame and the lab frame are opposite, the sign should be reversed. On making this sign reversal, we have a relation between the shock frame and the lab frame as $v_s = v_1$

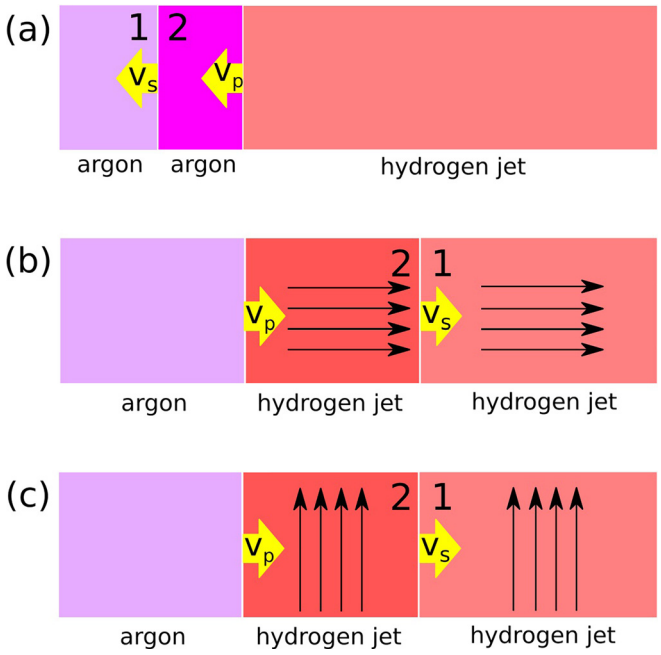

FIG. 13. (a) A HD shock forming in the argon gas cloud, (b) a parallel MHD shock forming in the hydrogen jet, and (c) a perpendicular MHD shock forming in the hydrogen jet. 1 and 2, respectively, indicate the unshocked and shocked regions. The black arrows indicate the direction of the magnetic field.

and $v_p = v_1 - v_2$. Details can be found in Ref. 30 the notations of which are used here. Here, we only consider $\gamma = 5/3$.

First, a HD shock can form in the argon gas cloud as illustrated in Fig. 13(a). If the jet velocity quickly slows down to 20 km/s, the mean free path also drops to ~2 cm so the jet could act like a rigid piston. Here, a strong shock is assumed because the jet velocity greatly exceeds the sound velocity in the argon gas cloud which will be shown below. In this condition, we can estimate the shock velocity using Eq. (14.135) of Ref. 30 given as $M_s \simeq (\gamma+1)M_p/2$, where $M_s = v_s/v_{c1}$ is the Mach number of the shock, where $v_{c1} = 0.3$ km/s is the sound speed in the argon gas cloud. The unshocked argon gas cloud (region 1) is assumed to be at room temperature ($T_1 = 300$ K). $M_p = v_p/v_{c1}$ is the Mach number of the jet. So, we have $M_s = M_1 \simeq 90$ which confirms the strong shock assumption and $v_s \simeq 4v_p/3 \simeq 27$ km/s from which displacement between the jet and the shock for 1 μs is 0.7 cm. This is not resolvable using our diagnostics. The velocities in the lab and shock frames are summarized in Table I. In the strong shock limit of the HD shock, the jump condition would give a very large increase in temperature while the density increase is limited to be less than a factor of 4 ($(\rho_2/\rho_1)_{\max} = (\gamma+1)/(\gamma-1) = 4$). The HD jump condition gives[30]

$$\frac{\rho_2}{\rho_1} = \frac{(\gamma+1)M_1^2}{2+(\gamma-1)M_1^2}, \tag{14}$$

$$\frac{p_2}{p_1} = \frac{1-\gamma+2\gamma M_1^2}{\gamma+1}, \tag{15}$$

$$= \frac{-\gamma+1+(\gamma+1)\rho_2/\rho_1}{(\gamma+1)-(\gamma-1)\rho_2/\rho_1}. \tag{16}$$

Using Eq. (16) and $T_2/T_1 = p_2\rho_1/(p_1\rho_2)$ provide plots of (a) p_2/p_1 vs. ρ_2/ρ_1 and (b) T_2/T_1 vs. ρ_2/ρ_1 as shown in Fig. 14. The HD shock (orange dashed line) shows a sharper increase in T_2/T_1 than the adiabatic compression (blue solid line) as ρ_2/ρ_1 increases. Using $M_1 = 90$ gives $T_2/T_1 \simeq 2500$. Since we assumed that $T_1 = 0.025$ eV, $T_2 \simeq 63$ eV is predicted by the shock model. However, we did not see any spectroscopic evidence of highly ionized argon ions in the experiment as would be expected for such a high temperature. Because the degree of ionization is mainly determined by the electron temperature, substantial ion heating by a shock could occur without the argon becoming highly ionized. For this to happen, the ion-electron equipartition time would have to be much larger than the ion shock heating time. Future study would thus require a two-fluid treatment[31] to determine the extent to which ions are shock heated.

Second, a parallel or perpendicular MHD shock can form in the jet if the frame-reversed gas cloud velocity ($v_p = 70$ km/s) exceeds the magnetosonic speed ($v_{MS} = \sqrt{v_A^2 + v_{c1}^2}$) in the jet as in the configurations shown in Figs. 13(b) and 13(c). Since the Alfvén speed in the jet is ≃26 km/s, where B ≃0.24 T and $n_e \simeq 4\times10^{22}$ m^{-3} and the sound speed in the jet is $v_{c1} \simeq 20$ km/s, the magnetosonic speed is ~32 km/s. We

TABLE I. A summary of velocities in HD and MHD shocks.

(a) Hydrodynamic shock (positive position is on the left)

	Unshocked Ar	Shock	Shocked Ar	H jet (piston)
Lab frame velocity	$v_1' = 0$ km/s	$v_s = 27$ km/s	$v_2' = 20$ km/s	$v_p = 20$ km/s
Shock frame velocity[a]	$v_1 = 27$ km/s	0 km/s	$v_2 = 7$ km/s	$v_{p,s}$[b] $= 7$ km/s

(b) Parallel and perpendicular MHD shock (positive position is on the right)

	Ar (piston)	Shocked H jet	Shock	Unshocked H jet
Frame reversed lab frame velocity[c]	$v_p = 70$ km/s	$v_2' = 70$ km/s	$v_s = 80$ km/s[d]	$v_1' = 0$ km/s
Shock frame velocity[a]	$v_{p,s} = 10$ km/s	$v_2 = 10$ km/s	0 km/s	$v_1 = 80$ km/s

[a]Sign is reversed.
[b]$v_{p,s}$ is the piston speed in the shock frame.
[c]The jet frame is regarded as a lab frame.
[d]$v_s = 80$ km/s is assumed for providing an example with actual numbers.

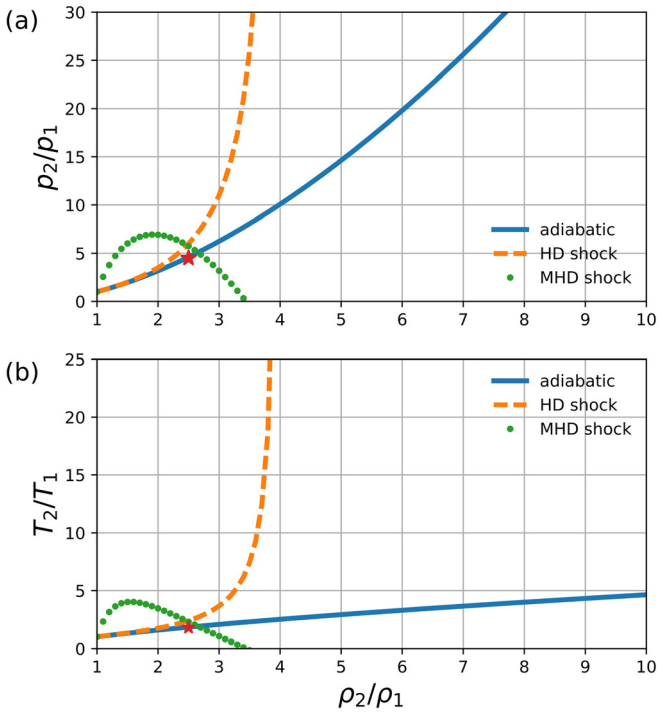

FIG. 14. Plots of (a) p_2/p_1 vs. ρ_2/ρ_1 (b) T_2/T_1 vs. ρ_2/ρ_1 for adiabatic compression, HD shock (or parallel MHD shock), and perpendicular MHD shock. The red star indicates the Caltech experimental results.

should note the Alfvén speed is a function of the magnetic field and density which have spatial dependence in the experiment and that B $\simeq$ 0.24 T is a maximum value of the jet on the axis. Thus, the initial frame-reversed gas cloud velocity satisfies the MHD shock condition. Also, the mean free path of argon neutral atoms penetrating into the hydrogen jet is small so as to act like a piston; the mean free path $l_{mfp} = 1/(n_i\sigma_{ni}) = 0.13$ cm, where $n_i = 4\times10^{16}\,\mathrm{cm}^{-3}$ is the ion density in the jet and $\sigma_{ni}(T_i = 25\,\mathrm{eV}) = 1.9\times10^{-16}\,\mathrm{cm}^{-2}$ is the argon neutral-hydrogen ion momentum transfer collision cross-section.[19] In the experimental configuration, the density and temperature measured by Thomson scattering were obtained at the geometrical axis where the z-component of the magnetic field is dominant. On-axis interaction can thus be approximated as a parallel MHD shock configuration which is identical to the HD shock.

A parallel shock condition ($\mathbf{v} \parallel \mathbf{B}$) gives no magnetic field compression meaning $B_2/B_1 = 1$. In this configuration, we cannot make a strong shock limit approximation. Instead, we can estimate a minimum $(M_1)_{\min}$ and $(T_2/T_1)_{\min}$ because $M_s > M_p$, where $M_p = v_p/v_{c1}$ is the piston Mach number. M_p will be used as a minimum Mach number. Substituting M_1 with $M_p = 3.5$ in the HD shock jump condition gives $(\rho_2/\rho_1)_{\min} = 3.2$, $(p_2/p_1)_{\min} = 15.1$, and $(T_2/T_1)_{\min} \simeq 4.8$. The observed electron density ($\rho_2/\rho_1 \simeq 2.5$) and temperature ($T_2/T_1 \simeq 1.8$) are not as high as the density and temperature predicted from the jump condition. The temperature predicted with the experimental result of $(\rho_2/\rho_1)_{\min} = 2.5$ also gives a higher temperature ratio $(T_2/T_1)_{\min} \simeq 2.4$ than the observation.

The perpendicular MHD ($\mathbf{v}\perp\mathbf{B}$) shock may be weak and located away from the geometrical axis where the magnetic field perpendicular to the flow is dominant. The jump condition of the perpendicular MHD shock gives[32]

$$\frac{p_2}{p_1} = 1 + \gamma M_1^2(1-(\rho_2/\rho_1)^{-1}) + \beta_1^{-1}(1-(\rho_2/\rho_1)^2), \quad (17)$$

where β_1 is the ratio of the thermal pressure to the magnetic pressure in the region 1. Equation (17) is shown in Fig. 14 as green dots using $(M_1)_{\min} = 3.5$ and $\beta_1 = 0.7$. Here, $\beta_1 = 0.7$ is obtained using $n_i = 4\times10^{22}$ m^{-3}, $T_i = 2.5$ eV, and B $\simeq$ 0.24 T which were measured at the geometrical axis. Since as a radial position increases the magnetic field and the electron density decreases, $\beta_{1,\mathrm{on-axis}} \simeq \beta_{1,\mathrm{off-axis}}$ is assumed. Using Eq. (17) gives

$$\frac{T_2}{T_1} = \frac{p_2}{p_1}\frac{\rho_1}{\rho_2} = \frac{1+\gamma M_1^2(1-(\rho_2/\rho_1)^{-1}+\beta_1^{-1}(1-(\rho_2/\rho_1)^2)}{\rho_2/\rho_1} \quad (18)$$

from which we have $(T_2/T_1)_{\min} \simeq 2.3$. Also, the jet velocity quickly drops to 20 km/s so the MHD shock condition may not be sustained.

In the case of weak compression there could exist ambiguity whether the compression is shock or adiabatic as shown in Fig. 14. In actual MTF, however, adiabatic compression and heating dominates shock compression because shock compression is limited to be less than a factor of $\rho_2/\rho_1 = 4$, while the compression ratio of MTF is $\rho_2/\rho_1 \simeq 1380$.

V. CONCLUSION

Compression and heating were observed when an MHD-driven jet impacted a gas target cloud. The goal of this jet-target experiment was to investigate adiabatic compression using a non-destructive and repeatable setup; besides being of fundamental interest, adiabatic compression is also relevant to magnetized target fusion. Comprehensive measurements showed increases in density and magnetic field and a decrease in jet velocity during the compression. The electron temperature had a rather complicated time dependence; the temperature increased at first and then dropped very quickly in a time less than 1 μs which is much shorter than the total compression time. The temperature drop can be understood as a result of radiative loss from three-body recombined hydrogen atoms. This three-body recombination is a dominant process in cool, high density plasmas and to avoid this issue, the compression would have to be faster than the radiative loss time. A criterion for the compression time with respect to the radiative loss was presented for the fusion-grade regime. $\gamma = 5/3$ is used to estimate the scaling of adiabatic compression based on the collisionality which would be an additional criterion for MTF-relevant systems. The results were also analyzed in the context of shocks the effects of which are compared to adiabatic compression.

ACKNOWLEDGMENTS

The authors would like to thank Dr. Amelia Greig at Cal Poly San Luis Obispo for her effort on the preliminary jet-impact experiment when working at Caltech as a

postdoctoral fellow. The authors would also like to acknowledge useful discussions with Dr. Hui Li at the Los Alamos National Laboratory; Dr. Li developed numerical models which are related to this experiment and which will be reported elsewhere. This research was supported by USDOE ARPA-E Grant No. DE-AR0000565.

[1]J. H. Degnan, D. J. Amdahl, A. N. Brown, T. Cavazos, S. K. Coffey, M. Domonkos, M. H. Frese, S. D. Frese, D. Gale, C. Gilman, C. Grabowski *et al.*, IEEE Trans. Plasma Sci. **36**, 80 (2008).
[2]M. Hohenberger, P. Y. Chang, G. Fiksel, J. P. Knauer, R. Betti, F. J. Marshall, D. D. Meyerhofer, F. H. Séguin, and R. D. Petrasso, Phys. Plasmas **19**, 056306 (2012).
[3]T. Intrator, S. Y. Zhang, J. H. Degnan, I. Furno, C. Grabowski, S. C. Hsu, E. L. Ruden, P. G. Sanchez, J. M. Taccetti, M. Tuszewski *et al.*, Phys. Plasmas **11**, 2580 (2004).
[4]S. A. Slutz, M. C. Herrmann, R. A. Vesey, A. B. Sefkow, D. B. Sinars, D. C. Rovang, K. J. Peterson, and M. E. Cuneo, Phys. Plasmas **17**, 056303 (2010).
[5]M. R. Gomez, S. A. Slutz, A. B. Sefkow, D. B. Sinars, K. D. Hahn, S. B. Hansen, E. C. Harding, P. F. Knapp, P. F. Schmit, C. A. Jennings *et al.*, Phys. Rev. Lett. **113**, 155003 (2014).
[6]G. A. Wurden, S. C. Hsu, T. P. Intrator, T. C. Grabowski, J. H. Degnan, M. Domonkos, P. J. Turchi, E. M. Campbell, D. B. Sinars, M. C. Herrmann *et al.*, J. Fusion Energy **35**, 69 (2016).
[7]I. R. Lindemuth and R. E. Siemon, AIP Conf. Proc. **1154**, 68 (2009).
[8]P. B. Parks, Phys. Plasmas **15**, 062506 (2008).
[9]S. C. Hsu and P. M. Bellan, Phys. Plasmas **12**, 032103 (2005).
[10]D. Kumar and P. M. Bellan, Phys. Rev. Lett. **103**, 105003 (2009).
[11]A. L. Moser and P. M. Bellan, Astrophys. Space Sci. **337**, 593 (2012).
[12]X. Zhai, H. Li, P. M. Bellan, and S. Li, Astrophys. J. **791**, 40 (2014).
[13]S. You, G. S. Yun, and P. M. Bellan, Phys. Rev. Lett. **95**, 045002 (2005).
[14]J. Sheffield, D. Froula, S. H. Glenzer, and N. C. Luhmann, Jr., *Plasma Scattering of Electromagnetic Radiation: Theory and Measurement Techniques* (Academic Press, 2010).
[15]B. Seo and P. M. Bellan, Rev. Sci. Instrum. **88**, 123504 (2017).
[16]C. A. Romero-Talamas, P. M. Bellan, and S. C. Hsu, Rev. Sci. Instrum. **75**, 2664 (2004).
[17]J. Howard, B. W. James, and W. I. B. Smith, J. Phys. D: Appl. Phys. **12**, 1435 (1979).
[18]B. P. Leblanc, Rev. Sci. Instrum. **79**, 10E737 (2008).
[19]IAEA, https://www-amdis.iaea.org/ALADDIN/ for ALADDIN Numerical Database.
[20]P. M. Bellan, Am. J. Phys. **72**, 679 (2004).
[21]D. R. Bates, Proc. R. Soc. London Ser. A **267**, 297 (1962).
[22]D. R. Bates and A. E. Kingston, Planet. Space Sci. **11**, 1 (1963).
[23]J. Cooper, Rep. Prog. Phys **29**, 35 (1966).
[24]E. Hinnov and J. Hirschberg, Phys. Rev. **125**, 795 (1962).
[25]D. Lumma, J. L. Terry, and B. Lipschultz, Phys. Plasmas **4**, 2555 (1997).
[26]Y. Nakai, T. Shirai, T. Tabata, and R. Ito, At. Data Nucl. Data Tables **37**, 69 (1987).
[27]NIST, https://www.nist.gov/pml/atomic-spectra-database for NIST Database.
[28]Thorlabs, https://www.thorlabs.com/thorproduct.cfm?partnumber=PDA36A for *Thorlabs* PAD-36A.
[29]U. Shumlak, B. A. Nelson, E. L. Claveau, E. G. Forbes, R. P. Golingo, M. C. Hughes, R. J. Oberto, M. P. Ross, and T. R. Weber, Phys. Plasmas **24**, 055702 (2017).
[30]R. Fitzpatrick, *Theoretical Fluid Mechanics* (IOP Publishing, 2017).
[31]M. Y. Jaffrin and R. F. Probstein, Phys. Fluids **7**, 1658 (1964).
[32]R. Fitzpatrick, *Plasma Physics: An Introduction* (CRC Press/Taylor & Francis Group, 2014).